Molecular Intercalation and Cohesion of Organic Bulk Heterojunction Photovoltaic Devices

*Christopher Bruner, Nichole C. Miller, Michael D. McGehee, and Reinhold H. Dauskardt**

The phase separated bulk heterojunction (BHJ) layer in BHJ polymer:fullerene organic photovoltaic devices (OPV) are mechanically weak with low values of cohesion. Improved cohesion is important for OPV device thermomechanical reliability. BHJ devices are investigated and how fullerene intercalation within the active layer affects cohesive properties in the BHJ is shown. The intercalation of fullerenes between the side chains of the polymers poly(3,3‴-didocecyl quaterthiophene) (PQT-12) and poly(2,5-bis(3-hexadecylthiophen-2-yl)thieno[3,2-b]thiophene (pBTTT) is shown to enhance BHJ layer cohesion. Cohesion values range from ≈1 to 5 J m^{-2}, depending on the polymer:fullerene blend, processing conditions, and composition. Devices with non-intercalated BHJ layers are found to have significantly reduced values of cohesion. The resulting device power conversion efficiencies (PCE) are also investigated and correlated with the device cohesion.

1. Introduction

Most studies on organic photovoltaic (OPV) reliability and degradation of cell performance have been primarily concerned with device failure mechanisms due to photo-oxidation and morphological stability of the active layers as well as electrochemical degradation at the electrode interfaces.[1–10] However failure modes related to mechanical stresses together with the inherently mechanically fragile nature of OPV layers remain generally unexplored and a limitation for OPV reliability.[11,12] For instance, the fragile nature of OPV films have implications for device yield during manufacturing and it has also been shown that inclement weather can damage encapsulation allowing for mechanical failure within the active OPV layers themselves during service.[10,13,14] Mechanical properties have been shown to govern device yield in large-scale manufacturing of other thin-film technologies and improved long-term reliability has been critically dependent on optimization of mechanical properties along with reduction of thin-film stresses.[14–22]

Recent studies have investigated the cohesive and adhesive properties of bulk heterojunction (BHJ) OPV devices with standard and inverted configurations with active layers prepared via spin-coating and roll-to-roll (R2R), respectively.[11,12] The primary active layer materials used in these studies were poly-(3-hexylthiophene-2,5-diyl) (P3HT): phenyl-C61-butyric acid methyl ester ($PC_{60}BM$). The phase separated BHJ layer in the standard device structure and the adjoining interfaces with the BHJ layer in the case of the inverted structure were mechanically the weakest, with comparatively low values of layer cohesion or interface adhesion, respectively. Such low fracture properties may result in mechanically fragile device structures that ultimately lead to low yield during device fabrication and reduce reliability during subsequent operation. These studies further demonstrated that layer compositions and processing conditions can significantly affect cohesion and adhesion values which provide opportunities to optimize materials and processing conditions to improve reliability.

In the present study, we investigate OPV devices prepared using spin-coating and show how fullerene intercalation within the active layer affects the cohesive properties in the OPV device structure. The fullerene derivative phenyl-C71-butyric acid methyl ester ($PC_{71}BM$) has been shown to intercalate between the side chains of the donor polymers poly(3,3‴-didodecyl quaterthiophene) (PQT-12) and poly(2,5-bis(3-hexadecylthiophen-2-yl)thieno[3,2-b]thiophene with C16 side chains (pBTTT) allowing for the formation of a bimolecular crystal phase.[23–27] We hypothesized that the formation of such a phase may enhance the mechanical cohesion of the BHJ layer. The cohesion of these devices was determined by characterizing the critical strain energy release rate, G_c needed to separate the BHJ layer. Cohesion of the BHJ layer ranged between ≈1 to 5 J m^{-2} depending on processing conditions and composition. The effects of processing conditions and morphology on the cohesion and device power conversion efficiencies (PCE) were also investigated.

2. Results and Discussion

2.1. X-Ray Diffraction

High-resolution specular X-ray diffraction data was collected on PQT-12:$PC_{71}BM$ and PQT-12:bis-$PC_{71}BM$ and is shown in **Figure 1**a. In agreement with published work that explored

C. Bruner, Dr. N. C. Miller, Prof. M. D. McGehee, Prof. R. H. Dauskardt
Department of Materials Science and Engineering
496 Lomita Mall, Durand Building, Stanford, CA 94305-2205, USA
E-mail: dauskardt@stanford.edu

DOI:10. 1002/adfm.201202969

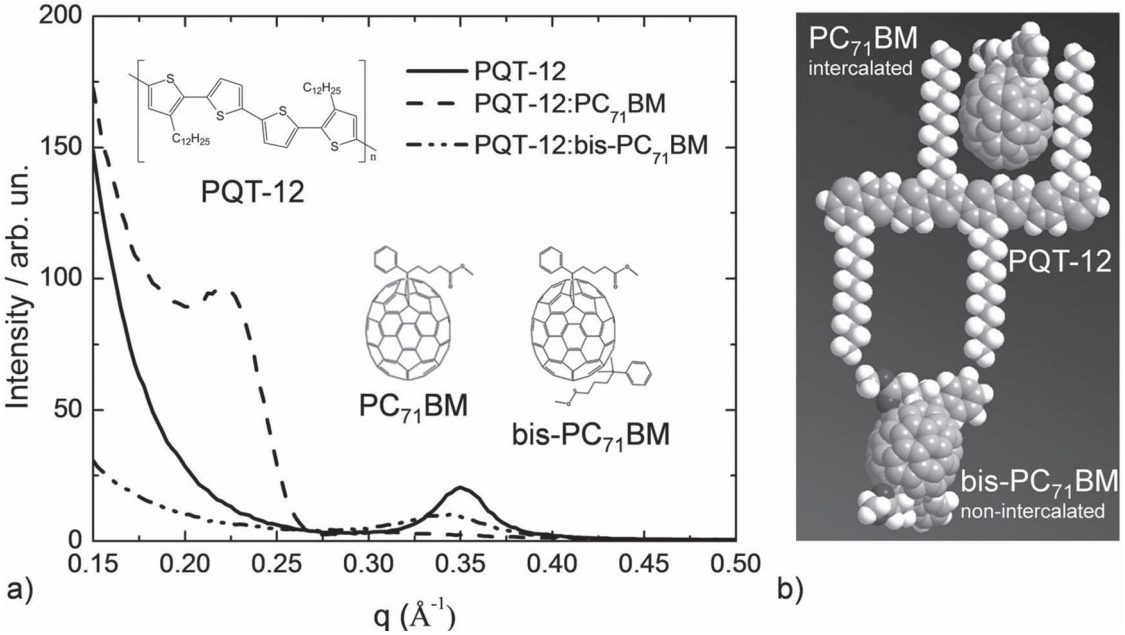

Figure 1. a) X-ray diffraction pattern for indicated polymer:fullerene films. Consistent with published data, we see an expasion in the d-spacing when going from a pure PQT-12 film to a PQT-12:PC$_{71}$BM film indicating that molecular intercalation has occurred.[23] From this work, we show that films made with PQT-12:bis-PC$_{71}$BM, the shift does not occur if at all, indicating intercalation has not occurred. b) A space-filling model made in Chem-3D of PQT-12, PC$_{71}$BM, and bis-PC$_{71}$BM for relative spatial comparison and to indicate how intercalation occurs for PC$_{71}$BM and not for bis-PC$_{71}$BM.

intercalation with PQT-12:PC$_{60}$BM blends, we see an expansion in the d-spacing with the addition of PC$_{71}$BM to PQT-12, from 17.95 Å to 28.24 Å.[23] However, with the addition of bis-PC$_{71}$BM to PQT-12, no similar expansion occurs which indicates that bis-PC$_{71}$BM (18.21 Å) does not intercalate between the PQT-12 side chains. This may be due to steric hindrance of the additional side group. We graphically demonstrate this in Figure 1b.

These results are not surprising considering previous work, which showed that PC$_{71}$BM intercalated between the side chains of the similar polymer poly(2,5-bis(3-hexadecylthiophen-2-yl)thieno[3,2-b]thiophene with C16 side chains (pBTTT-C16) whereas bis-PC$_{71}$BM does not.[26] Therefore, we assume an intercalated bimolecular crystal phase forms in the PQT-12:PC$_{71}$BM blends, whereas the PQT-12:bis-PC$_{71}$BM blends form regions of pure polymer and pure fullerene, although a molecularly mixed or intercalated amorphous region may also exist in these blends.[26–28]

2.2. Cohesion of Intercalated Organic Photovoltaic Devices

The cohesion values, G_c, of all PQT-12 and pBTTT-C14 OPVs measured using the four-point bend (FPB) cohesion technique are summarized in **Figure 2**. Previously reported cohesion of P3HT:PC$_{60}$BM are included for comparison.[11] Cohesion ranged between 1 and 5 J m^{-2} and were affected by intercalation. The intercalated BHJ layers (using PC$_{71}$BM) had a significantly greater cohesion compared to their non-intercalated (using bis-PC$_{71}$BM) counterparts when using a polymer:fullerene mass ratio of 1:1. The non-intercalated 1:1 polymer:fullerene devices generally possessed a much lower $G_c \approx 1$ J m^{-2}. For devices with a polymer:fullerene mass ratio of 1:4, cohesion values were significantly reduced for the

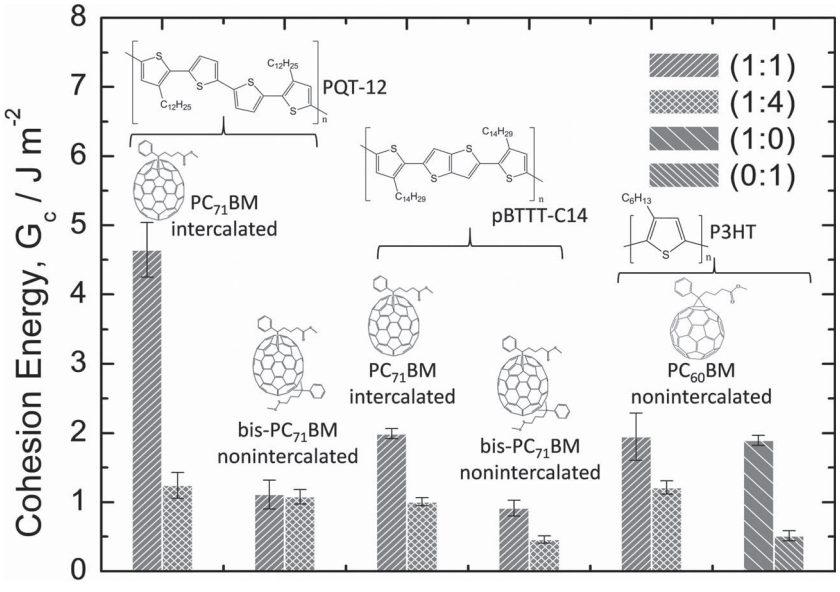

Figure 2. Comparison of internal cohesive fracture energy of the BHJ layer with indicated polymer:fullerene compositions and mass ratio compared to P3HT:PC$_{60}$BM cohesion values from previously published data.[11]

intercalated layers with $G_c \approx 1$ J m^{-2}. The non-intercalated layers again showed a decreased G_c value, particularly for the pBTTT-C14:bis-PC$_{71}$BM layer which was only ≈0.5 J m^{-2}. This indicates that even with intercalation, if a significant portion of the BHJ layer consists of pure fullerene domains, the cohesion and related resistance to mechanical failure will decrease. This is unfortunate since pure fullerene domains are necessary to produce a percolating pathway of fullerenes for electron transport to the cathode as the intercalated phase can only locally conduct electrons. Additionally, this evidence supports previous work with P3HT:PC$_{60}$BM devices which hypothesized that domains of PC$_{60}$BM form a relatively weak region due to low van der Waals interactions, which facilitates facile crack propagation during debonding.[11]

All of the devices failed within the active layer and characterization of the debond surfaces using XPS revealed elemental compositions of ≈90–92 at% carbon, 6–9 at% sulfur, and 0–4 at% oxygen. Depth profiling was used to infer the location of the debond path within the BHJ layer (Table S1, Supporting Information). The debond path predominantly occurred within the BHJ layer but close to the BHJ/PEDOT:PSS interface. Atomic force microscopy (AFM) images of the debond surfaces (**Figure 3**) revealed that a significantly greater surface roughness for the intercalating PQT-12:PC$_{71}$BM layer (R_q = 14.0 nm), which also exhibited a markedly higher G_c value.

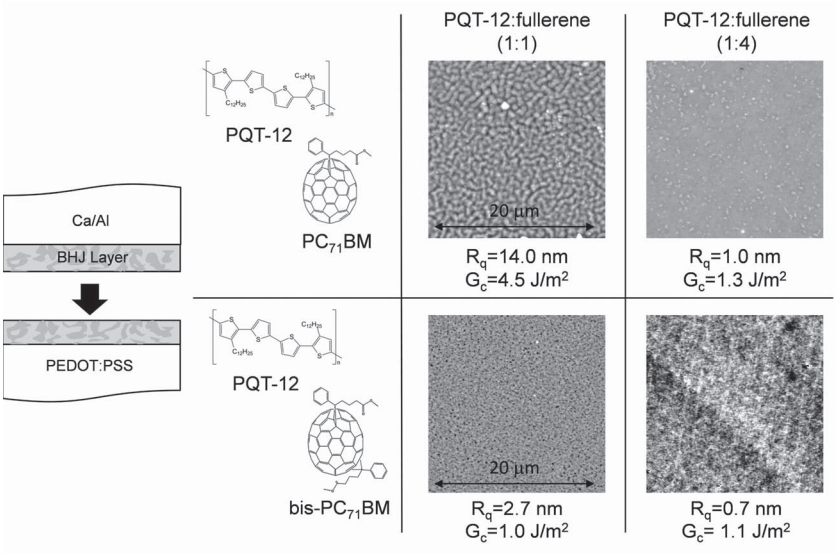

Figure 3. AFM scans for the debond surface attached to the PEDOT:PSS layer with indicated BHJ layer composition and polymer:fullerene ratios indicated. These scans indicate that relatively smooth samples correlate with lower cohesion.

To explain the increased cohesion of the intercalated layers, we note that for polymers that allow for fullerene intercalation, a 1:1 polymer:fullerene mass ratio produces only a bimolecular crystal phase.[27] For devices using pBTTT-C14, at temperatures below 225 °C, the bimolecular crystal phase readily forms indicative of the thermodynamic stability of the phase.[29] This stability suggests an increase in the favorable molecular interactions between the intercalated polymer and fullerene molecules and are related in the cohesive strength (Figure S1, Supporting Information). In addition, the rough debond surface, as revealed by AFM, may indicate that the debond path meanders along the bimolecular crystals phase (Figure 3). We see the significant increase in cohesion for 1:1 intercalated layers because the bimolecular crystal phase is sampled and not the weak fullerene domains.

In previous work with P3HT:PC$_{60}$BM, it was hypothesized that the polarity of the PC$_{60}$BM within the relatively less polar P3HT would minimize interactions between the two phases and thus lower cohesion.[11] In this work, we hypothesize that the additional side chain in bis-PC$_{71}$BM which increases the relative polarity of the fullerene further decreases favorable interactions between the fullerene and the polymer phase. Research on blends of P3HT:bis-PC$_{60}$BM have demonstrated an absence of large fullerene domains due to steric hindrance from the two side chains of the fullerene which limit its diffusion and crystallization.[30] This could mean that bis-PC$_{71}$BM which is sterically bulky, avoids aggregating into large domains while minimizing interactions with the polymer phase, thus taking up a greater degree of free volume. Free volume can act as a weak region from which defects can evolve into facile propagating cracks. Similar behavior has been suggested for defect formations in metallic glasses.[31–33]

2.3. Effect of Thermal Annealing on Cohesion for PQT-12 Devices

We have found that post-production annealing significantly enhanced device cohesion regardless of BHJ composition (**Figure 4**). We compare the effects of annealing for PQT-12 to that reported for P3HT:PC$_{60}$BM at 150 °C.[11] For all devices, a maximum cohesion value was found after 0.5 h of annealing, after which cohesion either remained unchanged or slightly decreased. The maximum cohesion after 0.5 to 1 h annealing was ≈5.9 J m^{-2} for PQT-12:PC$_{71}$BM (1:1), ≈2.5 J m^{-2} for PQT-12:PC$_{71}$BM (1:4), ≈4.2 J m^{-2} for PQT-12:bis-PC$_{71}$BM (1:1), ≈2.4 J m^{-2} for PQT-12:bis-PC$_{71}$BM (1:4), and ≈3.4 J m^{-2} for P3HT:PC$_{60}$BM.

Investigation of the surface topography of the debond surfaces with AFM revealed that with increasing annealing times, the average roughness increased (**Figure 5** and Figure S2, Supporting Information). This trend was also observed in previous work.[11] The increased roughness and cohesion of the BHJ layer can be explained as follows. For devices with non-intercalating BHJ layers, thermal annealing promotes the formation of crystalline polymer and fullerene domains.[34–37] Additionally, it is well-known that thermal annealing of PQT-12 above its glass transition temperature (140 °C) causes PQT-12 to become liquid-crystalline; a well-ordered phase can be achieved by slowly cooling from this liquid-crystalline phase. The PQT-12 can form π–π stacks with side chain interdigitation between neighboring PQT-12 chains.[24,38–40] It is possible that the greater degree of

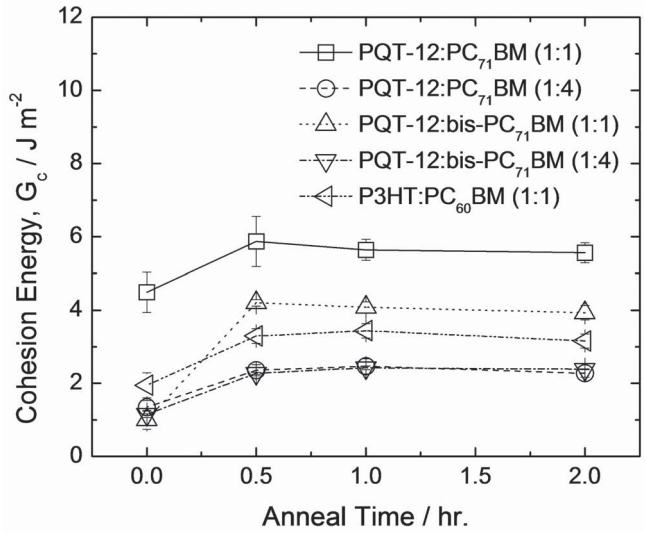

Figure 4. Cohesive energy versus anneal time. Each curve represents at least three specimens from the same OPV device with indicated BHJ layer composition annealed for the indicated amount of time at 150 °C. The maximum cohesion for each device was reached after half an hour of annealing with the exception of P3HT:PC_{60}BM (1:1), which peaked after 1 h. All additional annealing resulted in a decrease in device cohesion. All annealing took place post-production.

intermolecular side chain interdigitation also contributes to the increase in cohesion. Since failure is expected to occur around the polymer domains in the weaker fullerene regions, the increase in size of the different domains with annealing will cause the crack to deflect more creating a rougher surface. This agrees with our AFM analysis which indicated greater surface roughness with longer annealing times. The increase in fracture surface roughness results in an increase in cohesion not only due to an increase in crack surface area, but also deflection of the crack away from the plane of highest tensile loading.[15,41]

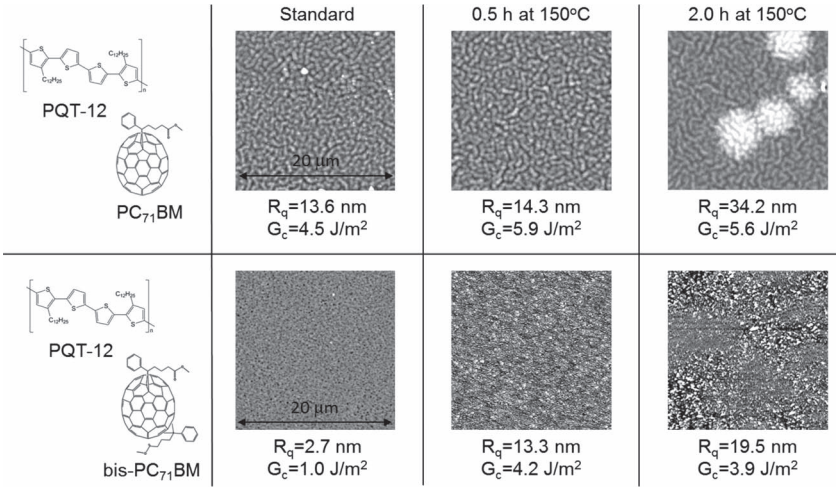

Figure 5. AFM scans of debond surfaces for 1:1 PQT-12:PC_{71}BM and 1:1 PQT-12:bis-PC_{71}BM as a function of postproduction annealing time. The AFM scans reveal that the coarsening of the surface morphology generally correlates to an increase in cohesion. All devices failed in the middle of the BHJ layer.

For devices with intercalating BHJ layers, the increase in cohesion may also be due to an increasing crystalline order of the intercalated phase.[26] Long thermal anneals for devices made using pBTTT-C14 and PQT-12 have noted very stable morphologies in the BHJ layer with no phase separation occurring.[23,24] The thermal annealing may also promote fullerene migration into the polymer phase, increasing the domain size of the intercalated phase. With the intercalated phase increasing in crystallinity and size, we would expect an increase in cohesion.

Additionally, we observed that for all annealed devices, the debond path occurs in the center of the BHJ layer. This therefore suggests the fracture resistance of the bottom of the BHJ layer has increased. This may be related to fullerene segregation towards the top of the layer and away from the PEDOT:PSS interface increasing the fullerene content in the upper part of the layer.[42] Thermal annealing also may facilitate an electrochemical reaction between the polymer in the active layer and PSS, thus forming a more fracture resistant $polymer^{+}$:PSS^{-} interfacial layer that increases cohesion near the PEDOT:PSS interface.[11,43]

It is interesting that the cohesion energy evolves with annealing time in almost exactly the same way for all of the 1:4 polymer-fullerene blends. This indicates that when there is high fullerene loading in the BHJ layer, the fullerene domains strongly dictate the cohesive properties of the layer. We suspect that the mechanisms which produced the increase in device cohesion for the 1:1 polymer:fullerene blend films apply to 1:4 polymer:fullerene blends, but the contribution to cohesion is less pronounced.

2.4. Device Cohesion and Efficiency

The current-voltage measurements for PQT-12 solar cells under AM 1.5 conditions that were annealed for different times with varying polymer to fullerene mass ratios (1:1 or 1:4) for fullerene acceptors PC_{71}BM and bis-PC_{71}BM are shown in **Figure 6**. We summarize the best performance for these cells in **Table 1**. Annealing was done at 150 °C, above the glass transition temperature of PQT-12, in order to ensure crystallization of the PQT-12 domains.[24,38–40] It is clear from all graphs that with increasing annealing times, we see a decrease in device performance due primarily to a decreasing short-circuit current density (J_{SC}). It must be noted that the goal was not to determine the optimal conditions for maximizing electronic properties but to see how processing that enhances mechanical properties affects device performance. We correlate the cohesion of these active layers with their PCE and J_{SC} in **Figure 7**.

For 1:1 PQT-12:PC_{71}BM, we see the least amount of J_{SC} loss was observed with increasing annealing time. For intercalated devices using a 1:1 polymer to fullerene mass ratio, essentially only the hole-conducting bimolecular crystal phase which is thermally

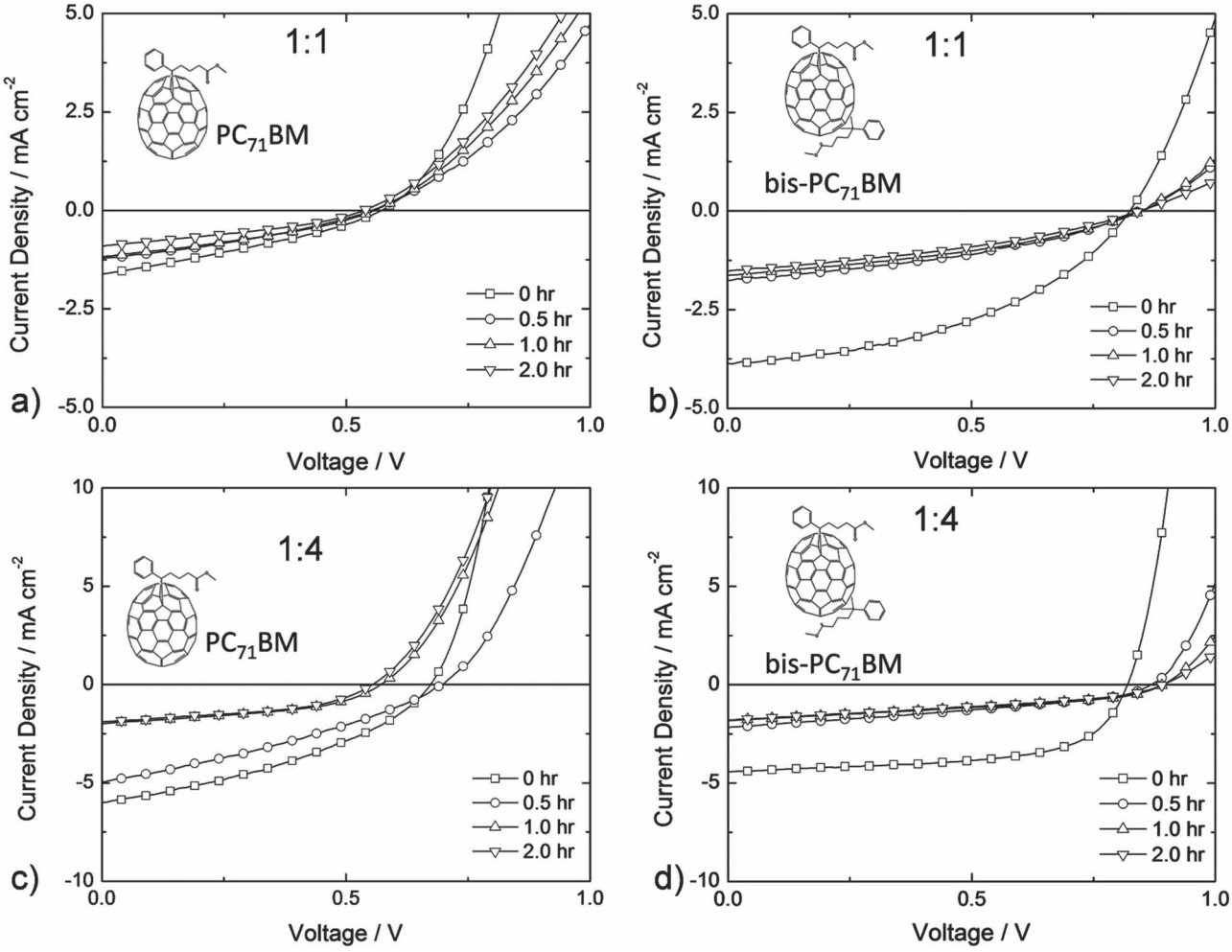

Figure 6. Current vs. voltage plots for PV devices under AM 1.5 illumination using the donor polymer PQT-12 with the following fullerenes and polymer:fullerene mass ratios: a) $PC_{71}BM$ (1:1), b) bis-$PC_{71}BM$ (1:1), c) $PC_{71}BM$ (1:4), and d) bis-$PC_{71}BM$ (1:4). Annealing took place postproduction at 150 °C for the amounts of time as indicated.

stable, exists.[23] Any fullerenes not already within the intercalated phase may rearrange during thermal annealing in order to intercalate between polymer side chains therefore reducing the number of available pathways for electron transport to the cathode.[23] This may help explain the observed drop in J_{SC} before for PQT-12 devices annealed at temperatures above 140 °C.[24] Also of interest, for all intercalated devices V_{OC} decreased with increasing annealing time. This may be due to the fact that as PQT-12 rearranges to form larger crystals (increased π–π stacking) when cooling, increasing π–π intermolecular interactions shifts the position of the highest occupied molecular orbital (HOMO) level and lower unoccupied molecular orbital (LUMO) level.[24,44,45] It has also been shown that a decrease in V_{OC} may be associated with greater polymer/fullerene interactions which would be consistent with a greater degree of fullerene intercalation.[44]

For 1:1 PQT-12:bis-$PC_{71}BM$, we observed a drop in J_{SC} and a reduced fill factor (FF) after half an hour of annealing and no further losses with increasing annealing time. This unusual result can be explained by the fact that most anneal treatments that showed improved device performance typically occurred for short time scales on the order of 5 to 10 min.[24,46–49] For non-intercalated phase-separated bulk heterojunction devices, thermal annealing helps the formation of polymer crystallites thus improving absorbance and allows for vertical phase segregation of the fullerenes allowing for better charge transport.[42,50] However, with increasing annealing times, it is possible that fullerenes in the mixed phase region will drop below the percolation threshold leaving a discontinuous network of fullerenes that can act as recombination centers reducing charge collection. This rationalization for the observed decrease in J_{SC} can also be extended to 1:4 PQT-12:bis-$PC_{71}BM$. Additionally we observe an increase in V_{OC} for all non-intercalated devices with increasing annealing time. Even with a greater degree of π–π intermolecular interactions between polymer chains, as the fullerene acceptors aggregate away from the polymer phase, weaker polymer/fullerene interactions may lead to a larger V_{OC}.[44,45]

For 1:4 PQT-12:$PC_{71}BM$, we see an initial drop in J_{SC} after half an hour; after one hour of annealing, we witness no further

Table 1. Best photovoltaic device performance under AM 1.5 conditions measured for given active layer composition as a function of annealing time at 150 °C.

Active Layer Composition	Polymer:Fullerene Mass Ratio	Anneal Time [h]	V_{oc} [mV]	J_{sc} [mA/cm^2]	FF	$\eta_{e\ (AM\ 1.5)}$ [%]
PQT-12:$PC_{71}BM$	1:1	0	575	1.62	0.3	0.28
		0.5	555	1.21	0.33	0.22
		1.0	555	1.18	0.33	0.22
		2.0	535	0.90	0.34	0.16
PQT-12:$PC_{71}BM$	1:4	0	645	6.59	0.38	1.63
		0.5	695	4.97	0.33	1.12
		1.0	575	1.99	0.44	0.50
		2.0	555	1.88	0.46	0.48
PQT-12:bis-$PC_{71}BM$	1:1	0	815	3.95	0.51	1.66
		0.5	865	1.72	0.38	0.57
		1.0	865	1.64	0.39	0.54
		2.0	855	1.57	0.36	0.48
PQT-12:bis-$PC_{71}BM$	1:4	0	815	4.44	0.61	2.21
		0.5	865	2.17	0.35	0.66
		1.0	895	1.82	0.38	0.61
		2.0	895	1.80	0.36	0.58

significant drop. It has been observed by others that for intercalated systems with 1:4 polymer:fullerene mass ratios that annealing devices can lead to a decrease in performance due to a decrease in electron mobility.[23] This decrease has been attributed to aggregation of the fullerenes which results in discontinuous pathways for electron conduction.[37]

In summation, we observe a decrease in device performance due to postproduction annealing but generally an increase in active layer cohesion. Challenges to future design will include finding an optimum combination of PCE and G_c to maximize OPV reliability and cost. We note that manufacturing methods such as spin-coating and roll-to-roll (R2R) with subsequent annealing are known to play an important role in cohesive/adhesive strength.[11,12,51,52] Understanding the effects of these large-scale manufacturing methods will be important. The present study has shown the importance of molecular intercalation and annealing on OPV device mechanical properties. A more focused study looking at internal device morphology and utilizing computational modeling may be required to further probe the interplay of these two properties.

3. Conclusions

The cohesion for organic photovoltaic devices incorporating the polymers PQT-12 and pBTTT-C14 have been studied. Failure occurs cohesively within the BHJ layer and is affected by the formation of a bimolecular crystal phase within the BHJ layer when PQT-12 or pBTTT-C14 are combined with the fullerene derivative $PC_{71}BM$. The BHJ layer cohesion is also strongly linked to the amount of fullerenes within the active layer regardless of what polymer is used, where high amounts of fullerene produce a very weak layer.

It was shown that thermal annealing of the devices can increase cohesion by a factor of four. This increase in BHJ cohesion was the result of a number of factors including the formation of larger polymer domains in the non-intercalated devices, the formation of an interlayer between the BHJ layer and PEDOT:PSS, and increased crystalline order of the intercalated phase in the BHJ layer. Additionally, by analyzing the debond surfaces of the FPB specimens, we observed an increasing surface roughness with increasing annealing time perhaps indicating that polymer and fullerene crystallite formation allows for greater crack tip deflection, thereby increasing cohesion.

Finally, we observed an increase in the BHJ layer cohesion with thermal annealing corresponded to a reduced PCE for all devices due to a significant decrease in J_{SC}. This decrease in J_{SC} most likely came about from greater recombination due to a decrease in interfacial regions between the hole-transport phase (polymer phase in non-intercalated devices, the bimolecular crystal phase in intercalated devices) and the electron- transport phase (fullerenes) with increasing individual domain size from thermal annealing.

4. Experimental Section

OPV Device Preparation: OPVs for mechanical testing were fabricated on 50 mm × 50 mm squares of 0.7 mm thick borosilicate glass substrates with an indium tin oxide (ITO) coating (20 Ω sq^{-1}, Patterned ITO, Thin Film Devices). Devices for current-voltage testing were simultaneously fabricated but built on similar glass substrates but with patterned ITO. Substrates were cleaned in an ultrasonic bath with Extran 300 (4-EX0996-20-EA, Krackeller Scientific), rinsed in deionized water, and then treated with UV ozone. Poly(3,4-ethylenedioxythio-phene):poly(styrenesulfonate) (PEDOT:PSS) (Baytron) was spin-coated on the ITO at 2000 rpm with an acceleration of 1000 rpm/s for 30 s and the substrates were annealed at 150 °C for 10 min to evaporate the water. They were then transferred

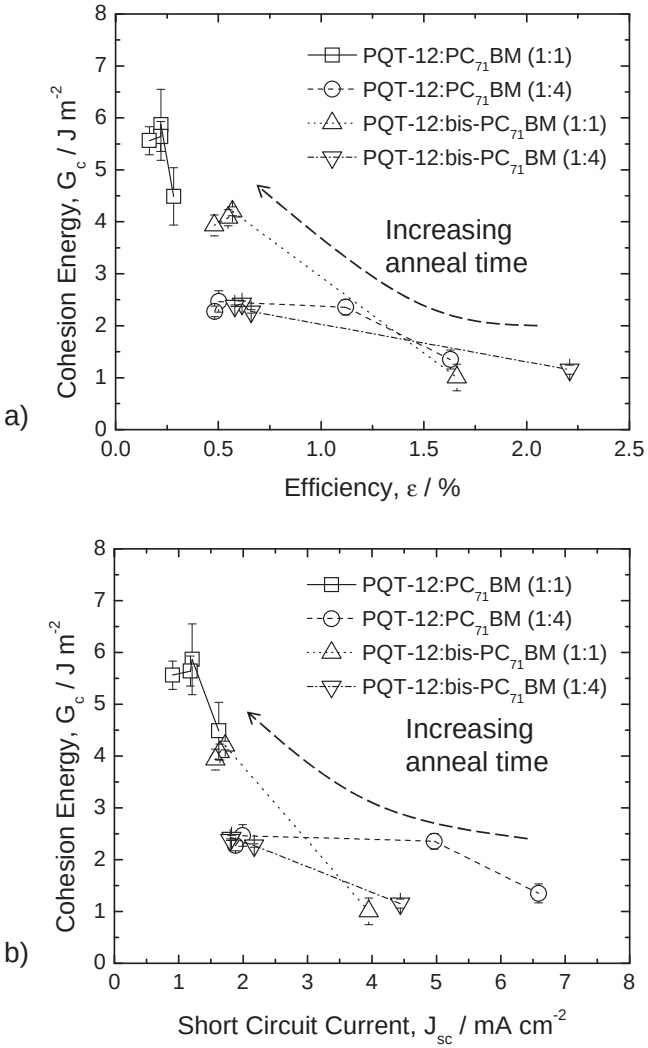

Figure 7. a) Each curve represents the fracture energy for an OPV device vs. maximum PCE for the given active layer composition and polymer:fullerene mass ratio. From right to left, each point for a given curve represents fracture energy and PCE for a given anneal time with anneal temperature 150 °C starting from 0 h to 2.0 as described in the experimental section. b) These curves display the fracture energy vs. the J_{SC} for the devices with the highest PCE. Anneal times start from 0 h to 2.0 from left to right.

to a nitrogen glovebox (OMNI, Vacuum Atmospheres, Hawthorne, CA, USA), where they remained for the duration of the fabrication process.

The BHJ layer ($PC_{71}BM$, bis-$PC_{71}BM$, Nano-C and PQT-12, American Dye Source, Inc. and pBTTT-C14, Solarmer) was spin coated on the PEDOT:PSS layer at 900 rpm with an acceleration of 500 rpm/s for 45 s. The BHJ for PQT-12 devices was cast using chlorobenzene and 25 mg of solute per 1 mL of solvent, after stirring ≈12 h at 70 °C. For pBTTT-14 devices, the BHJ was cast using ortho-dichlorobenzene and 25 mg of solute per 1 mL of solvent, after stirring ≈12 h at 90 °C. All devices were allowed to slow dry ≈12 h. Finally, Ca and Al metal electrodes (Ca pieces and Al pellets, Kurt J. Lesker Company) were deposited in a thermal evaporator (hand built) on the active layer. The active area for current-voltage tested PV devices was 0.1 cm^2. Additional specimens for X-ray diffraction analyses were prepared by spin coating the BHJ layer using dichlorobenzene 20 mm × 20 mm × 0.7 mm silicon substrates.

Active Layer Thickness Measurement: The BHJ thickness was measured for each device with a profilometer (Dektak 150+ Surface Profiler, Veeco). The depth of a controlled scratch was measured on a portion of the OPV that had not been coated with Ca and Al, so that each measurement gave the combined thickness of the PEDOT:PSS and the BHJ layers. To extract the BHJ layer thickness, a separate measurement was made on ITO coated glass that only had the PEDOT:PSS layer on it. Thickness values were determined by averaging at least three measurements (Table S2, Supporting Information).

Postproduction Annealing: Three devices of each solar cell composition using the polymer PQT-12 were annealed at 150 °C (just above the polymers glass transition temperature) in a nitrogen glovebox for 0.5, 1.0 and 2.0 h.[24] Their adhesion/cohesion were measured subsequently.

Adhesion/Cohesion Specimen Preparation: For adhesion/cohesion testing, an identical glass substrate was glued onto the Al layer of the fabricated OPV with a brittle epoxy (Epo-Tek 353ND, Epoxy Technology). The resulting photovoltaic sandwich structure was cured for 1 h at 90 °C to harden the epoxy and the edges were sealed with another epoxy (Loctite E-20NS, Hysol) to prevent diffusion of water and air into the OPV sandwich during dicing. To produce individual specimens with dimensions 4 mm × 50 mm × 1.4 mm, 0.6 mm deep trenches were cut on each side of the structure using a wafer saw with a resin blade, and then specimens were cleaved into individual specimens prior to testing. A pre-notch was machined at the top center of each specimen, approximately two-thirds the depth of the top glass beam.[15,53] Three specimens from each OPV device were used for quantifying the cohesion of the structure by means of the FPB sampling technique.

Adhesion/Cohesion Testing: To measure adhesion and cohesion the four-point bend (FPB) method was employed where the specimens were loaded under displacement control with a displacement rate of 0.25 μm/s and a moment arm, *L*, of 6.5 mm in a high resolution micromechanical testing system (DTS, Menlo Park, CA, USA).[15] The critical load, P_c, that causes crack propagation, was determined from the plateau of the load-displacement curve, occurring during stable crack extension. The cohesion of the layer (also known as fracture energy or fracture resistance), G_c, was calculated as the critical value of the strain energy release rate, as defined by:[15,54]

$$G_c = \frac{21 P_c^2 L^2}{16 b^2 h^3 E'} \quad (1)$$

where *E″* is the biaxial modulus and *b* and *h* are the specimen width and half-height, respectively. The FPB specimen has a mixed mode loading configuration with a phase angle of $\psi = 43°$. A schematic for the FPB test specimen is given in Figure S3a (Supporting Information) and further details are given elsewhere.[15] During testing the crack may extend as much as 10 mm, ≈40 mm^2 of the layer or interface, making the resulting measurement statistically significant.

Surface Analysis: After adhesion/cohesion testing, X-ray photoelectron spectroscopy (XPS) (PHI VersaProbe XPS Microprobe, Physical Electronics, Chanhassen, MN, USA) was performed to chemically characterize the resulting debond surfaces to identify the debond path. The XPS system utilized the Al K_α radiation and a hemispherical analyzer and position sensitive detector, with an energy resolution of ≈1 eV. The beam spot size was 100 × 100 μm^2 and the detection angle was 35°. A low-energy electron flood gun was also used to reduce any charging of the specimen during analysis. Specialized software was used to identify peaks and compositional analysis.[55] In addition, atomic force microscopy (AFM) (XE-70 microscope, Park Systems, Santa Clara, CA, USA) was used to characterize the morphology of the debond surfaces in the non-contact mode and average roughness (R_q) was recorded.

X-Ray Diffraction Analysis: Specular X-ray diffraction was performed at beamline 2-1 at the Stanford Synchrotron Radiation Lightsource with an X-ray energy of 8 keV. The X-ray diffraction intensity was collected as a function of the scattering vector, $q = 2\pi/d$, where *d* is the *d*-spacing for the diffracting planes.

Current–Voltage Measurements: Photovoltaic current–voltage measurements were conducted in the glove box where devices were

fabricated. Current-voltage measurements were measured with a source meter (Keithley 2400) and a solar simulator (Spectra-Physics 91160-1000) under 1 sun (AM 1.5G) using an NREL certified KG-5 filtered silicon diode.

Supporting Information

Supporting Information is available from the Wiley Online Library or from the author.

Acknowledgements

This work was partly supported by the Director, Office of Energy Research, Office of Basic Energy Sciences, Materials Sciences Division of the U.S. Department of Energy, under contract no. DE-FG02-10ER46391 and by the Center for Advanced Molecular Photovoltaics (CAMP) supported by King Abdullah University of Science and Technology (KAUST) under award no. KUS-C1-015-21. Portions of this research were carried out at the Stanford Synchrotron Radiation Lightsource, a national user facility operated by Stanford University on behalf of the US Department of Energy, Office of Basic Energy Sciences.

Received: October 12, 2012
Revised: November 21, 2012
Published online: January 17, 2013

[1] C. H. Peters, I. T. Sachs-Quintana, J. P. Kastrop, S. Beaupre, M. Leclerc, M. D. McGehee, *Adv. Energy Mater.* **2011**, *1*, 491.
[2] C. H. Peters, I. T. Sachs-Quintana, W. R. Mateker, T. Heumueller, J. Rivnay, R. Noriega, Z. M. Beiley, E. T. Hoke, A. Salleo, M. D. McGehee, *Adv. Mater.* **2012**, *24*, 663.
[3] J. Alstrup, K. Norrman, M. Jorgensen, F. C. Krebs, *Sol. Energy Mater. Sol. Cells* **2006**, *90*, 2777.
[4] Y. M. Sun, C. J. Takacs, S. R. Cowan, J. H. Seo, X. Gong, A. Roy, A. J. Heeger, *Adv. Mater.* **2011**, *23*, 2226.
[5] M. T. Lloyd, C. H. Peters, A. Garcia, I. V. Kauvar, J. J. Berry, M. O. Reese, M. D. McGehee, D. S. Ginley, D. C. Olson, *Sol. Energy Mater Sol. Cells* **2011**, *95*, 1382.
[6] S. Bertho, G. Janssen, T. J. Cleij, B. Conings, W. Moons, A. Gadisa, J. D'Haen, E. Goovaerts, L. Lutsen, J. Manca, D. Vanderzande, *Sol. Energy Mater. Sol. Cells* **2008**, *92*, 753.
[7] G. Griffini, J. D. Douglas, C. Piliego, T. W. Holcombe, S. Turri, J. M. J. Frechet, J. L. Mynar, *Adv. Mater.* **2011**, *23*, 1660.
[8] J. Vandenbergh, B. Conings, S. Bertho, J. Kesters, D. Spoltore, S. Esiner, J. Zhao, G. Van Assche, M. M. Wienk, W. Maes, L. Lutsen, B. Van Mele, R. A. J. Janssen, J. Manca, D. J. M. Vanderzande, *Macromolecules* **2011**, *44*, 8470.
[9] N. Grossiord, J. M. Kroon, R. Andriessen, P. W. M. Blom, *Org. Electron.* **2012**, *13*, 432.
[10] M. Jorgensen, K. Norrman, S. A. Gevorgyan, T. Tromholt, B. Andreasen, F. C. Krebs, *Adv. Mater.* **2012**, *24*, 580.
[11] V. Brand, C. Bruner, R. H. Dauskardt, *Sol. Energy Mater. Sol. Cells* **2012**, *99*, 182.
[12] S. R. Dupont, M. Oliver, F. C. Krebs, R. H. Dauskardt, *Sol. Energy Mater. Sol. Cells* **2012**, *97*, 171.
[13] F. C. Krebs, H. Spanggard, T. Kjaer, M. Biancardo, J. Alstrup, *Mater. Sci. Eng. B* **2007**, *138*, 106.
[14] H. F. Nied, *IEEE Trans. Device Mater. Res.* **2003**, *3*, 129.
[15] R. Dauskardt, M. Lane, Q. Ma, N. Krishna, *Eng. Fract. Mech.* **1998**, *61*, 141.
[16] J. J. Vlassak, Y. Lin, T. Y. Tsui, *Mater. Sci. Eng. A* **2005**, *391*, 159.
[17] S. Y. Kook, J. M. Snodgrass, A. Kirtikar, R. H. Dauskardt, *J. Electron. Packag.* **1998**, *120*, 328.
[18] T. S. Kim, N. Tsuji, K. Matsushita, N. Kobayashi, D. Chumakov, H. Geisler, E. Zschech, R. H. Dauskardt, *J. Appl. Phys.* **2008**, 104.
[19] R. H. Dauskardt, B. M. Sharratt, L. C. Wang, *Acta Mater.* **2007**, *55*, 3601.
[20] C. S. Litteken, R. H. Dauskardt, *Int. J. Fracture* **2003**, *119*, 475.
[21] S. Y. Kook, R. H. Dauskardt, *J. Appl. Phys.* **2002**, *91*, 1293.
[22] E. P. Guyer, R. H. Dauskardt, *Nat. Mater.* **2004**, *3*, 53.
[23] A. C. Mayer, M. F. Toney, S. R. Scully, J. Rivnay, C. J. Brabec, M. Scharber, M. Koppe, M. Heeney, I. McCulloch, M. D. McGehee, *Adv. Funct. Mater.* **2009**, *19*, 1173.
[24] P. Vemulamada, G. Hao, T. Kietzke, A. Sellinger, *Org. Electron.* **2008**, *9*, 661.
[25] N. C. Cates, R. Gysel, J. E. P. Dahl, A. Sellinger, M. D. McGehee, *Chem. Mater.* **2010**, *22*, 3543.
[26] N. C. Cates, R. Gysel, Z. Beiley, C. E. Miller, M. F. Toney, M. Heeney, I. McCulloch, M. D. McGehee, *Nano. Lett.* **2009**, *9*, 4153.
[27] N. C. Cates, R. Gysel, Z. Beiley, C. E. Miller, M. F. Toney, M. Heeney, I. McCulloch, M. D. McGehee, *Abstr. Pap. Am. Chem. Soc.* **2009**, 238.
[28] N. C. Cates, G. F. Burkhard, R. Gysel, Z. Beiley, E. T. Hoke, S. R. Scully, C. E. Miller, M. F. Toney, M. Heeney, I. McCulloch, M. D. McGehee, *Abstr. Pap. Am. Chem. Soc.* **2010**, 240.
[29] N. C. Miller, R. Gysel, C. E. Miller, E. Verploegen, Z. Beiley, M. Heeney, I. McCulloch, Z. N. Bao, M. F. Toney, M. D. McGehee, *J. Polym. Sci. Polym. Phys.* **2011**, *49*, 499.
[30] M. A. Faist, P. E. Keivanidis, S. Foster, P. H. Wobkenberg, T. D. Anthopoulos, D. D. C. Bradley, J. R. Durrant, J. Nelson, *J. Polym. Sci. Polym. Phys.* **2011**, *49*, 45.
[31] K. K. Cameron, R. H. Dauskardt, *Scripta Mater.* **2006**, *54*, 349.
[32] B. C. Menzel, R. H. Dauskardt, *Acta Mater.* **2006**, *54*, 935.
[33] C. A. Schuh, T. C. Hufnagel, U. Ramamurty, *Acta Mater.* **2007**, *55*, 4067.
[34] J. Jo, S. S. Kim, S. I. Na, B. K. Yu, D. Y. Kim, *Adv. Funct. Mater.* **2009**, *19*, 866.
[35] W. L. Ma, C. Y. Yang, X. Gong, K. Lee, A. J. Heeger, *Adv. Funct. Mater.* **2005**, *15*, 1617.
[36] M. Campoy-Quiles, T. Ferenczi, T. Agostinelli, P. G. Etchegoin, Y. Kim, T. D. Anthopoulos, P. N. Stavrinou, D. D. C. Bradley, J. Nelson, *Nat. Mater.* **2008**, *7*, 158.
[37] A. Swinnen, I. Haeldermans, M. vande Ven, J. D'Haen, G. Vanhoyland, S. Aresu, M. D'Olieslaeger, J. Manca, *Adv. Funct. Mater.* **2006**, *16*, 760.
[38] Y. O. Wu, P. Liu, B. S. Ong, T. Srikumar, N. Zhao, G. Botton, S. P. Zhu, *Appl. Phys. Lett.* **2005**, 86.
[39] M. I. M. Heeney, C. Bailey, K. Genevicius, M. I. M. Shkunov, D. Sparrowe, S. Tierney, R. Wagner, W. M. Zhang, M. L. Chabinyc, R. J. Kline, M. D. Mcgehee, M. F. Toney, *Nat. Mater.* **2006**, *5*, 328.
[40] L. H. Jimison, A. Salleo, M. L. Chabinyc, D. P. Bernstein, M. F. Toney, *Phys. Rev. B* **2008**, 78.
[41] M. Lane, W. Ni, R. H. Dauskardt, Q. Ma, H. Fujimoto, N. Krishna, *Thin Films: Stresses Mech. Prop.VII* **1998**, *516*, 357.
[42] A. J. Parnell, A. D. F. Dunbar, A. J. Pearson, P. A. Staniec, A. J. C. Dennison, H. Hamamatsu, M. W. A. Skoda, D. G. Lidzey, R. A. L. Jones, *Adv. Mater.* **2010**, *22*, 2444.
[43] D. M. Huang, S. A. Mauger, S. Friedrich, S. J. George, D. Dumitriu-LaGrange, S. Yoon, A. J. Moule, *Adv. Funct. Mater.* **2011**, *21*, 1657.
[44] M. D. Perez, C. Borek, S. R. Forrest, M. E. Thompson, *J. Am. Chem. Soc.* **2009**, *131*, 9281.

[45] K. Vandewal, K. Tvingstedt, A. Gadisa, O. Inganas, J. V. Manca, *Nat. Mater.* **2009**, *8*, 904.
[46] L. H. Nguyen, H. Hoppe, T. Erb, S. Gunes, G. Gobsch, N. S. Sariciftci, *Adv. Funct. Mater.* **2007**, *17*, 1071.
[47] G. Li, V. Shrotriya, Y. Yao, Y. Yang, *J. Appl. Phys.* **2005**, 98.
[48] F. Padinger, R. S. Rittberger, N. S. Sariciftci, *Adv. Funct. Mater.* **2003**, *13*, 85.
[49] T. Agostinelli, S. Lilliu, J. G. Labram, M. Campoy-Quiles, M. Hampton, E. Pires, J. Rawle, O. Bikondoa, D. D. C. Bradley, T. D. Anthopoulos, J. Nelson, J. E. Macdonald, *Adv. Funct. Mater.* **2011**, *21*, 1701.
[50] T. Erb, U. Zhokhavets, G. Gobsch, S. Raleva, B. Stuhn, P. Schilinsky, C. Waldauf, C. J. Brabec, *Adv. Funct. Mater.* **2005**, *15*, 1193.
[51] R. Sondergaard, M. Hosel, D. Angmo, T. T. Larsen-Olsen, F. C. Krebs, *Mater. Today* **2012**, *15*, 36.
[52] R. R. Sondergaard, M. Hosel, F. C. Krebs, *J. Polym. Sci. Polym. Phys. B* **2012**, *51*, 16.
[53] M. Lane, R. H. Dauskardt, N. Krishna, I. Hashim, *J. Mater. Res.* **2000**, *15*, 203.
[54] P. G. Charalambides, H. C. Cao, J. Lund, A. G. Evans, *Mech. Mater.* **1990**, *8*, 269.
[55] J. H. Scofield, *J. Electron. Spectrosc.* **1976**, *8*, 129.